2015-2569

Pressure Measurements of Burst Wakes Over a Three-Element Airfoil

Brent W. Pomeroy,* and Michael S. Selig†

University of Illinois at Urbana-Champaign, Department of Aerospace Engineering, Urbana, IL 61801

Wakes generated by a three-element high-lift multielement airfoil system, consisting of a main element and two flaps, were studied using a 7-hole probe in a low-speed wind tunnel. Strong adverse pressure gradients applied to a wake can cause off-the-surface separation in the wake, which is known as wake bursting. The tests were performed in the University of Illinois low-speed low-turbulence subsonic wind tunnel on a multielement airfoil having a baseline-configuration chord length of 1.36 ft (0.416 m) and a model span of 2.8 ft (0.85 m). Results are presented at a freestream Reynolds number of 1×10^6 for a variety of configurations in which the flaps were positioned in different locations. An increase in wake thickness was observed with decreased gap size, increased overhang distance, and increased flap deflection angle. An increase in angle of attack caused a thicker wake, but essentially no change in the minimum velocity observed in the wake.

Nomenclature

c	=	chord length
C_p	=	static pressure coefficient
$C_{p,t}$	=	total pressure coefficient
C_s	=	static pressure calibration coefficient
C_t	=	total pressure calibration coefficient
C_ϕ	=	roll angle calibration coefficient
C_θ	=	cone angle calibration coefficient
p	=	pressure
$\overline{p}$	=	mean static pressure of holes 1–6
q	=	dynamic pressure
U_t	=	magnitude of total velocity $\sqrt{u^2+v^2+w^2}$
u	=	chordwise velocity component
v	=	chord-normal velocity component
w	=	spanwise velocity component
x	=	Cartesian coordinate parallel to freestream flow
y	=	Cartesian coordinate orthogonal to freestream flow
α	=	angle of attack
β	=	sideslip angle
δ	=	flap deflection angle
μ	=	dynamic viscosity
ρ	=	density
ϕ	=	7-hole probe roll angle
θ	=	7-hole probe cone angle

Subscripts

l	=	pertaining to the lower portion of the wake
le	=	leading edge
n	=	parameter relating to element n

*Graduate Research Fellow, Department of Aerospace Engineering, 104 S. Wright St., AIAA Student Member.
†Associate Professor, Department of Aerospace Engineering, 104 S. Wright St., AIAA Associate Fellow.

$peak$ = point at which minimum $C_{p,t}$ is observed
s = static
t = total
u = pertaining to the upper portion of the wake
∞ = freestream conditions

Superscripts
$(\tilde{\ })$ = dimensionless value of variable
$(\bar{\ })$ = mean value of variable

I. Introduction

High-lift systems are integral to the low-speed performance of transport aircraft, and are necessary to achieve desired takeoff and landing metrics. Takeoff conditions require the aircraft to takeoff and climb to a given altitude in a minimum amount of time while burning as little fuel as possible. When landing an aircraft, it is desired to decrease the approach and landing speeds by increasing $C_{L,max}$ to minimize landing field length. Aerodynamic performance of a high-lift system can dramatically affect the performance parameters of the entire aircraft, as documented in a various trade studies. Preliminary design trade studies for a generic 150-passenger airplane with a range of 2,700 nm suggest a 5% increase in takeoff L/D results in an 11% increase in range for a given payload while a 5% increase in $C_{L,max}$ during landing yields a 20% increase in payload for a given approach speed.[1]

The aerodynamics of multielement high-lift devices is complex and can be greatly impacted by wakes in an adverse pressure gradient. In addition to the shape and location of each element, the wake of the main element, the jet through the gaps, and the flap wakes can all have a large effect on the flowfield.[2,3] If a strong adverse pressure gradient is imposed on a multielement airfoil, a wake may experience off-the-surface separation, or "wake bursting," while the flow along the surface remains attached. Wake bursting is a local deceleration of the flow in the wake of one or more of the elements. A conceptual sketch of a burst-wake region is presented in Fig. 1. As shown in the drawing, a wake from an element may rapidly thicken and decelerate because of the strong adverse pressure gradient. Both the main element wake and first flap wake are burst in the sketch. Burst wakes are characterized by rapid wake thickening, flow deceleration, and increased turbulence.[4–8] In general, aerodynamic performance of the airfoil is poorer if the wakes of the main element and the flaps become confluent, i.e. if they merge.

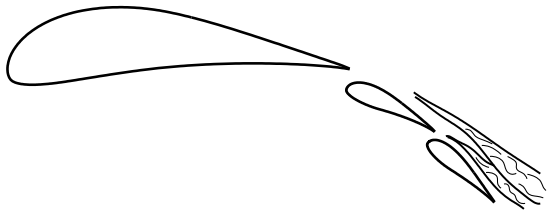

Figure 1. Conceptual sketch of wake bursting over a high-lift multielement airfoil.

Wake bursting, as discussed by Smith,[2] is a viscous phenomenon, leading to increased drag (C_d), a reduction of maximum lift $(C_{l,max})$, an effective decambering of the airfoil system, and sometimes flow reversal in the wake.[5,6,9,10] As expected, the pressure distribution of a multielement airfoil can be driven by the wakes in addition to the shape and location of the flap elements.[4,11–14] In fact, if the wakes merge, it has been shown that the momentum deficit in the wakes can dominate the flowfield.[12,15–19] Research performed in the NASA Langley Low Turbulence Pressure Tunnel (LTPT) indicated that the development of a wake is highly dependent on the Reynolds number of the flow and that a lower Reynolds number can result in larger wakes and more off-the-surface flow reversal.[11,19] Some previous tests investigated the burst wake of a flat plate with a single flap in an adverse pressure gradient imposed by moveable tunnel walls with no flow curvature.[10,20–22] These flat plate tests concluded that turbulence intensity and wake thickness both increased with a stronger adverse pressure gradient.

The objective of this study was to experimentally capture numerous burst wakes over a multielement airfoil and to determine different parameters which affect the formation and behavior of the burst wakes. Methods were implemented to capture wake formation and development over a large spatial region (more than 1.5 chord lengths downstream of

the trailing edge). Efforts were made to determine the effect of the airfoil geometry, specifically the flap position, on the wake behavior. Finally, the effect of angle of attack is documented.

II. Airfoil Geometry and Coordinate Systems

A three-element airfoil system, the MFFS(ns)-026, was examined in this research.[7,8,23] The airfoil, plotted in Fig. 2, is the same geometry that was used in previous research by the authors and is similar to the multielement system designed by Ragheb.[23] As seen in Fig. 2, the airfoil system is shown at $\alpha = 0$ deg with a system chord length of 1. It is defined that $\alpha = 0$ deg when the leading edge and trailing edge of the main element lie on the x axis as depicted. The system chord line is defined as the distance from the leading edge of the main element to the trailing edge of the last element projected along the main element chord line. Coordinates for each element are provided in Ref. 8.

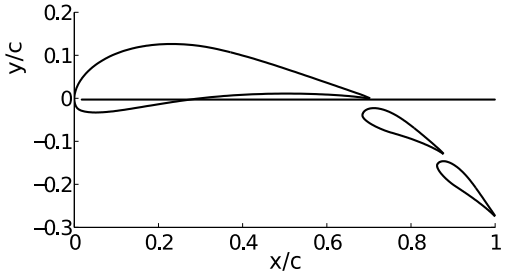

Figure 2. MFFS(ns)-026 three-element airfoil at $\alpha = 0$ deg.

Two coordinate systems were used to define the location of each element of the airfoil system including a relative and an absolute coordinate system. A relative coordinate system, as shown in Fig. 3(a), could be used to define the system by parameters that govern the flow including gap size, overhang distance, and relative deflection angle. The gap size between elements (gap_n) was defined as the distance from the trailing edge of element n to the closest point on element $n+1$. The overhang distance $(overhang_n)$ between element n and $n+1$ was defined as the distance from the leading edge of element $n+1$ to the trailing edge of n projected along the chord line of element n, as shown in the lower portion of Fig. 3(a). A positive overhang distance indicates the leading edge of element $n+1$ is upstream of the trailing edge of element n, as shown in the figure. Finally, the relative deflection angle (δ_r) for the two flaps was defined relative to the chord line of the previous element. The dimensional chord length of the main element (c_1) was 11.5 in (292 mm), the chord length of the first flap (c_2) was 3.5 in (88 mm), and the chord length of the second flap (c_3) was 3.0 in (76 mm). Nondimensional chord lengths were obtained by dividing the chord length of each element (c_n) by the system chord length (16.36 in for the baseline configuration). Results in this paper discuss five different configurations of the baseline MFFS(ns)-026 geometry plotted in Fig. 2 in which the two flaps were located in different positions. Each of these configurations isolated a change in a parameter of the relative coordinate system (*gap*, *overhang*, or δ_r) relative to the baseline configuration, Configuration 10. The flap locations for each configuration, as defined by the relative coordinate system, is presented in Table 1. A succinct description, or "purpose," of each configuration is also included in the table. These configurations were selected in an attempt to determine the effect of *gap*, *overhang*, and δ_r on the presence and behavior of the burst wakes.

The absolute coordinate system was used to define the location of each element in terms of the leading edge coordinate $(x,y)_{le,n}$ and deflection angle δ_n [see Fig. 3(b)]. Each element was thus located by the leading edge point of the airfoil element. As shown in the figure, the deflection angle of each flap element was defined relative to the main element chord line, and a positive deflection angle corresponded to a downward flap deflection. Table 2 presents the leading edge points and deflection angles for the five different configurations studied in this research. The configurations presented in Table 1 and 2 are identical, but defined in different coordinate systems in the two tables. The same trite description for each of these configurations is presented in the "Purpose" column.

III. Experimental Methods

Aerodynamic tests were performed in the University of Illinois low-speed low-turbulence wind tunnel as sketched in Fig. 4. The tunnel is an open-return-type wind tunnel, and the rectangular cross section is 2.8 ft (0.85 m) by 4.0 ft (1.22 m) and 8.0 ft (2.44 m) long. The downstream location of the test section is 0.5 in (1.3 cm) wider than the

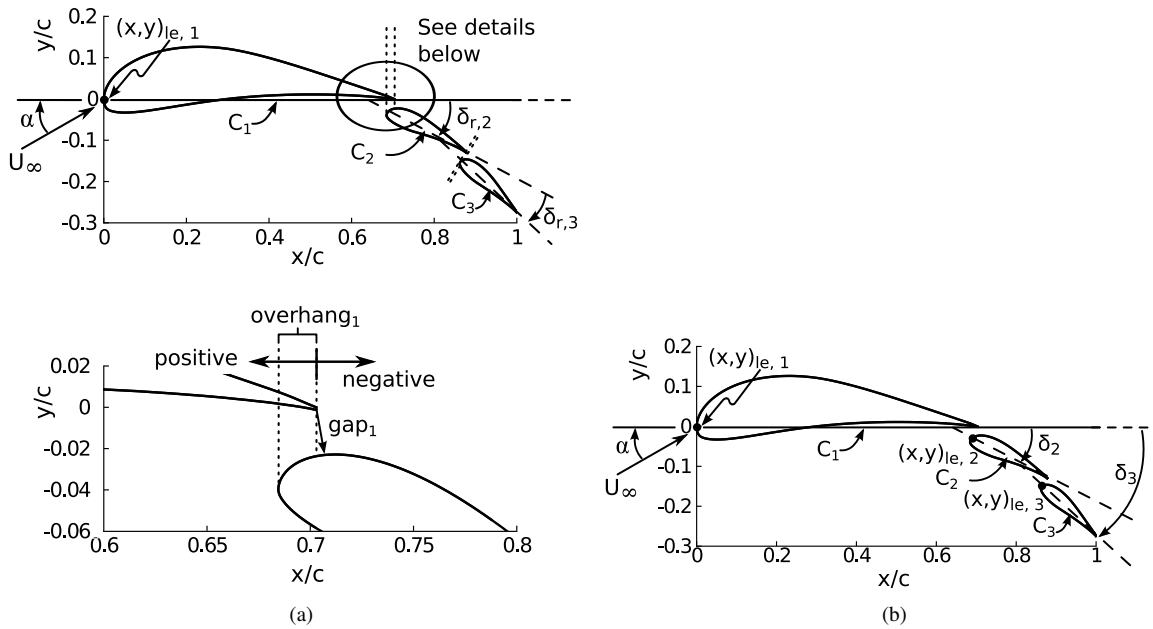

(a) (b)

Figure 3. Coordinate systems used to define the three-element airfoil geometry including a) relative coordinates and b) absolute coordinates.

Table 1. Location of Elements in Airfoil System in Relative Coordinates

Airfoil	Main Element to Flap 1			Flap 1 to Flap 2			
Configuration	gap_1	$overhang_1$	δ_r	gap_2	$overhang_2$	δ_r	Purpose
10	0.0100	0.0150	26.4 deg	0.0100	0.0150	15.9 deg	Baseline
11	0.0100	0.0150	22.0 deg	0.0100	0.0150	10.0 deg	Decreased δ
13	0.0100	0.0000	26.4 deg	0.0100	0.0000	15.9 deg	Decreased *overhang*
15	0.0200	0.0150	26.4 deg	0.0200	0.0150	15.9 deg	Increased *gap*
16	0.0050	0.0150	26.4 deg	0.0050	0.0150	15.9 deg	Decreased *gap*

Table 2. Location of Elements in Airfoil System in Absolute Coordinates

Airfoil	Flap 1		Flap 2		
Configuration	$(x,y)_{le}$	δ	$(x,y)_{le}$	δ	Purpose
10	$(0.6907, -0.0178)$	26.4 deg	$(0.8619, -0.1352)$	42.3 deg	Baseline
11	$(0.6724, -0.0195)$	22.0 deg	$(0.8478, -0.1150)$	32.0 deg	Decreased δ
13	$(0.6889, -0.0117)$	26.4 deg	$(0.8653, -0.1261)$	42.3 deg	Decreased *overhang*
15	$(0.6943, -0.0283)$	26.4 deg	$(0.8612, -0.1559)$	42.3 deg	Increased *gap*
16	$(0.6889, -0.0126)$	26.4 deg	$(0.8623, -0.1248)$	42.3 deg	Decreased *gap*

upstream end to account for boundary layer growth along the walls. To ensure good flow quality, the air passes through a 4 in (10.2 cm) thick honeycomb mesh, four stainless steel anti-turbulence screens, and a 7.5:1 inlet contraction. The presence of these screens and flow conditioning reduces the empty test section turbulence intensity to less than 0.1% at all operating speeds.[24] The speed of the tunnel was set by a five-blade metal fan driven by a 125 HP AC motor that was controlled by an ABB ACS 800 Low Voltage AC Drive. A maximum fan speed of 1,200 RPM creates a test section flow speed of approximately 165 mph (74 m/sec) or a maximum Reynolds number of 1.45×10^6/ft (4.75×10^6/m),

yielding a maximum Reynolds number of 1.98×10^6 for the current 16.36 in (1.35 ft, 0.416 m) chord model. The speed was computer controlled to maintain a desired Reynolds number during all tests reported in this paper. Standard methods were used to correct measurements of freestream velocity and dynamic pressure in the test section due to the presence of the model and wind tunnel walls.[25]

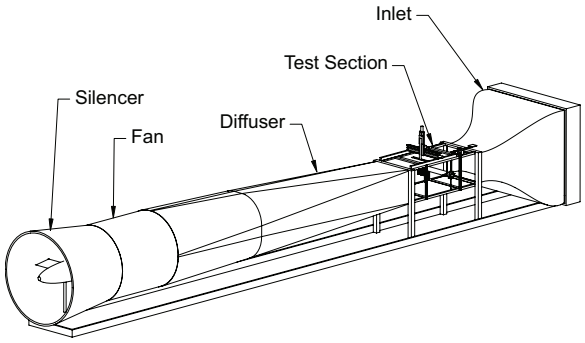

Figure 4. University of Illinois 2.8 × 4 ft low-speed low-turbulence subsonic wind tunnel.

A two-axis Lintech traverse system mounted to the sidewall of the tunnel, as shown in Fig. 5, was used to maneuver a 7-hole probe to various locations in the flowfield. This traverse system was modified to permit a maximum of 40 in (1.0 m) of upstream/downstream movement and 12 in (0.30 m) in the chord-normal direction. Two arms of the traverse passed through horizontal slots in the sidewall of the wind tunnel, and the 7-hole probe was mounted to the end of the traverse arm. A diagonal support (upper arm) was attached to the traverse for added structural integrity. An external symmetric airfoil fairing was used to streamline the traverse arms and minimize potential vibration from vortex shedding. The slots in the side of the wind tunnel were sealed using sliding acrylic panels which covered the slots at all times.

Figure 5. Sidewall-mounted traverse setup for current test.

Wake measurements were collected using an Aeroprobe 7-hole probe and a Pressure System DTC Initium with one ± 10 in water column (0.36 psi, 2.5 kPa) miniature electronically-scanned differential-pressure module. A 7-hole probe was chosen for the current study as it is possible to determine all three components of velocity (u, v, and w) in addition to static pressure (p), dynamic pressure (q), and total pressure (p_t) at the tip of the probe with good accuracy, even at high flow angles. After performing a calibration, methods can be implemented to determine the air speed, flow direction, static pressure, and total pressure.[26–31] As shown in Fig. 6(a,b), the total probe diameter was 0.125 in (3.18 mm) and consisted of six 0.020 in (0.51 mm) holes centered around one central hole of a 30 deg conical tip. Spatial averaging was avoided by limiting the step size in the direction along the probe centerline to 0.10 in (2.54 mm), which is larger than the 0.091 in (2.3 mm) length of the probe, and 0.125 in (3.18 mm) in the axis orthogonal to the probe centerline which is equal to the 0.125 in width of the probe [see Fig. 6(a)]. The probe was mounted in the wind tunnel such that holes 5 and 6 were located at the lowest y direction. Figure 6(c) shows the region sampled by the 7-hole probe relative to the baseline three-element airfoil (Configuration 10). Measurements were taken no closer

than 0.35 in (8.9 mm, 2.8 probe diameters) to the surface of the airfoil to reduce probe-airfoil interactions and to avoid collisions between the probe and the airfoil surface. As the wake surveys took approximately 6 hr to complete, methods were employed to decrease the run time and capture the most-relevant data. The wake domain was sampled with a step size in the streamwise direction (Δx) of 0.10 in (2.5 mm) close to the airfoil model and at a step size of 0.188 in (4.76 mm) in further downstream locations while the step size in y (Δy) was 0.125 in (3.18 mm) at all locations in the surveyed region. In addition, the downstream region was specified to capture the burst wake without capturing significant amounts of extraneous data. A spherical coordinate system (r, θ, ϕ) was used for the 7-hole probe, and the relationship between this coordinate system and the standard α-β coordinate system is shown in Fig. 6(d).

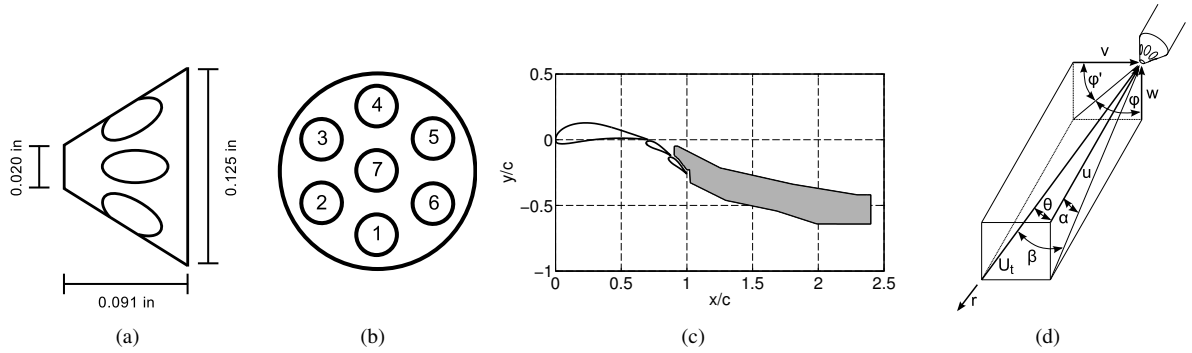

Figure 6. Details of 7-hole probe test including a) probe head geometry, b) hole layout, c) sample domain, and d) coordinate system.

A series of calibration coefficients were used to determine the flow angle, total pressure, and static pressure at the tip of the 7-hole probe by using a technique known as "sectoring." After a measurement was recorded, the hole with the highest pressure determined which sector, and thus which set of calibration equations, would be used. Each sector consists of four calibration coefficients in which each coefficient is dependent only upon the cone angle (θ), roll angle (ϕ), static pressure (p_s), and total pressure (p_t). If hole 7, the center hole, has the highest pressure, a set of coefficients, as derived by Gallington,[26] can be defined to be

$$C_a = \frac{p_1 - p_4}{p_7 - \overline{p}} \tag{1}$$

$$C_b = \frac{p_6 - p_3}{p_7 - \overline{p}} \tag{2}$$

$$C_c = \frac{p_5 - p_2}{p_7 - \overline{p}} \tag{3}$$

where

$$\overline{p} = \frac{1}{6}\sum_{i=1}^{6} p_i \tag{4}$$

The coefficients C_a, C_b, and C_c can be used to define a set of four additional calibration coefficients. This set of coefficients includes coefficients that are only sensitive to either pitch, yaw, total pressure, or static pressure, and are given by

$$C_{\theta_7} = \frac{1}{3}\left(2C_a + C_b - C_c\right), \qquad C_{\phi_7} = \frac{1}{\sqrt{3}}\left(C_b + C_c\right), \qquad C_{t_7} = \frac{p_7 - p_t}{p_7 - \overline{p}}, \qquad C_{s_7} = \frac{\overline{p} - p_s}{p_7 - \overline{p}} \tag{5}$$

Some cases exist for which hole 7 is not the hole with the highest pressure, but rather the highest pressure is measured by one of the outer holes. In these cases, the hole with the highest pressure and the three surrounding holes are used to determine the calibration coefficients, which can be expressed for sectors 1–6 as

$$C_{\theta_1} = \frac{p_1 - p_7}{p_1 - \frac{p_6+p_2}{2}}, \qquad C_{\phi_1} = \frac{p_6 - p_2}{p_1 - \frac{p_6+p_2}{2}}, \qquad C_{t_1} = \frac{p_1 - p_t}{p_1 - \frac{p_6+p_2}{2}}, \qquad C_{s_1} = \frac{\frac{p_6+p_2}{2} - p_s}{p_1 - \frac{p_6+p_2}{2}} \tag{6}$$

$$C_{\theta_2} = \frac{p_2 - p_7}{p_2 - \frac{p_1+p_3}{2}}, \qquad C_{\phi_2} = \frac{p_1 - p_3}{p_2 - \frac{p_1+p_3}{2}}, \qquad C_{t_2} = \frac{p_2 - p_t}{p_2 - \frac{p_1+p_3}{2}}, \qquad C_{s_2} = \frac{\frac{p_1+p_3}{2} - p_s}{p_2 - \frac{p_1+p_3}{2}} \tag{7}$$

$$C_{\theta_3} = \frac{p_3 - p_7}{p_3 - \frac{p_2+p_4}{2}}, \qquad C_{\phi_3} = \frac{p_2 - p_4}{p_3 - \frac{p_2+p_4}{2}}, \qquad C_{t_3} = \frac{p_3 - p_t}{p_3 - \frac{p_2+p_4}{2}}, \qquad C_{s_3} = \frac{\frac{p_2+p_4}{2} - p_s}{p_3 - \frac{p_2+p_4}{2}} \tag{8}$$

$$C_{\theta_4} = \frac{p_4 - p_7}{p_4 - \frac{p_3+p_5}{2}}, \qquad C_{\phi_4} = \frac{p_3 - p_5}{p_4 - \frac{p_3+p_5}{2}}, \qquad C_{t_4} = \frac{p_4 - p_t}{p_4 - \frac{p_3+p_5}{2}}, \qquad C_{s_4} = \frac{\frac{p_3+p_5}{2} - p_s}{p_4 - \frac{p_3+p_5}{2}} \tag{9}$$

$$C_{\theta_5} = \frac{p_5 - p_7}{p_5 - \frac{p_4+p_6}{2}}, \qquad C_{\phi_5} = \frac{p_4 - p_6}{p_5 - \frac{p_4+p_6}{2}}, \qquad C_{t_5} = \frac{p_5 - p_t}{p_5 - \frac{p_4+p_6}{2}}, \qquad C_{s_5} = \frac{\frac{p_4+p_6}{2} - p_s}{p_5 - \frac{p_4+p_6}{2}} \tag{10}$$

$$C_{\theta_6} = \frac{p_6 - p_7}{p_6 - \frac{p_5+p_1}{2}}, \qquad C_{\phi_6} = \frac{p_5 - p_1}{p_6 - \frac{p_5+p_1}{2}}, \qquad C_{t_6} = \frac{p_6 - p_t}{p_6 - \frac{p_5+p_1}{2}}, \qquad C_{s_6} = \frac{\frac{p_5+p_1}{2} - p_s}{p_6 - \frac{p_5+p_1}{2}} \tag{11}$$

It is noted that pressures in Eqs. 5-11 are absolute pressure. A set of calibrations were performed to determine the coefficients in Eqs. 5-11 as a function of known dynamic pressure, static pressure, roll angle, and cone angle. After the coefficients were determined, a series of lookup tables were employed to determine p_s, p_t, θ, and ϕ as a function of the four calibration coefficients. Six different velocities between 25 and 200 ft/sec (25, 50, 100, 150, 175, and 200 ft/sec) were tested to determine any Reynolds-number-dependent behavior of the probe, and calibrations were performed from a roll angle of 0 to 175 deg at 6 deg increments.

While calibrations were performed in the θ-ϕ coordinate system, flowfield measurements were desired in the α-β coordinate system. Based on the coordinate system shown in Fig. 6(d), it can be shown that

$$\alpha = \arcsin\left(\frac{\sin\theta\cos\phi}{\cos\beta}\right) \tag{12a}$$

$$\beta = \arcsin\left(\sin\theta\sin\phi\right) \tag{12b}$$

Because incompressible subsonic flow was assumed for the current research, which is valid because the maximum freestream Mach number was 0.10, the static, dynamic, and total pressure can be related at a single point in space by

$$p_t = p_s + q \tag{13}$$

where

$$q = \frac{1}{2}\rho U_t^2 \tag{14}$$

in which U_t is the magnitude of the velocity vector, the total velocity, as defined by

$$U_t = \sqrt{u^2 + v^2 + w^2} \tag{15}$$

Total velocity can be decomposed into u, v, and w by a series of rotation matrices in which

$$u = U_t\cos\alpha\cos\beta \tag{16a}$$

$$v = U_t\sin\beta \tag{16b}$$

$$w = U_t\sin\alpha\cos\beta \tag{16c}$$

The aforementioned calibration maps were used as lookup tables to determine the speed and direction of the local flow by using the 7-hole probe. Calibration coefficients were calculated for the appropriate sector based on the hole with the highest pressure by

$$\alpha = f_1(C_\theta, C_\phi) \tag{17a}$$

$$\beta = f_2(C_\theta, C_\phi) \tag{17b}$$

$$C_s = f_3(C_\theta, C_\phi) \tag{17c}$$

$$C_t = f_4(C_\theta, C_\phi) \tag{17d}$$

from which the static pressure and total pressure could then be found and used to calculate the dynamic pressure from which U_t was subsequently determined. Uncertainty in total velocity was determined to be 0.33 ft/sec (0.28% at a Reynolds number of 1×10^6) while the uncertainty in α and β were found to be 0.54 and 0.59 deg, respectively.

Methods were employed to nondimensionalize all values in this research. Nondimensional values are denoted by the tilde character ($\tilde{}$) which is placed over the corresponding letter or symbol. Cartesian coordinates were normalized by the airfoil chord length such that

$$[\widetilde{x},\widetilde{y}]^T = [x,y]^T/c \tag{18}$$

Velocity values, including U_t as well as u, v, and w were normalized by the freestream velocity, viz

$$[\widetilde{U_t},\widetilde{u},\widetilde{v},\widetilde{w}]^T = [U_t,u,v,w]^T/U_\infty \tag{19}$$

The static pressure was nondimensionalized by the standard equation

$$C_p = \frac{p - p_\infty}{q_\infty}, \tag{20}$$

while a similar nondimensionalization was applied to P_t in which the coefficient of total pressure $C_{p,t}$ was defined by

$$C_{p,t} = \frac{p_t - p_{t,\infty}}{q_\infty} \tag{21}$$

Thus, the nondimensional head loss at a given point relative to the freestream can be evaluated by Eq. 21.

IV. Results

Quantitative time-averaged aerodynamic flowfield data were acquired for a variety of freestream conditions for numerous different airfoil geometry configurations. Five different airfoil configurations (Configuration 10, 11, 13, 15, and 16), as defined in Table 1, were tested with various values of gap size, overhang distance, and relative flap deflection angle. Off-body pressure measurements were collected with a 7-hole probe at numerous different α values and freestream Reynolds numbers. Data that were calculated include flow speed, flow direction, static pressure, and total pressure.

A. Baseline (Configuration 10) Results

A baseline configuration for the three-element airfoil, referred to as Configuration 10, was tested at $\alpha = 0.0$ deg and $Re = 1.00 \times 10^6$. Data were collected for this condition, and nondimensional total velocity ($\widetilde{U_t}$), as defined by Eq. 19, is shown in Fig. 7; a wide view is shown in Fig. 7(a) while a detailed view is shown in Fig. 7(b) in which the downstream portion of flap 1 is visible and the entirety of flap 2 is visible. As seen in Fig. 7(a), data were collected between $\widetilde{x} = 0.90$ and $\widetilde{x} = 2.41$ at a range of $\widetilde{y}$ locations that was dependent upon the $\widetilde{x}$ location. This was done to decrease the run time of the experiments, which averaged approximately 6 hours each.

Wake bursting is evident in the flowfield plotted in Fig. 7, as evidenced by the thick wake in which a large momentum deficit is observed. The wake from the main element is visible in the upper-left corner of the plot [Fig. 7(b)]. Due to the size of the probe and the necessity to maintain adequate offset distance from the surface, only a small portion of the flap 1 wake is visible at ($\widetilde{x} \approx 0.95$, $\widetilde{y} \approx -0.20$) after which the flap 1 wake merges with the wake from the main element. The main element wake begins to rapidly thicken and burst at ($\widetilde{x} \approx 0.91$, $\widetilde{y} \approx -0.13$), and a minimum value of $\widetilde{U_t}$ of 0.69 is observed just downstream of the trailing edge of flap 2. The minimum velocity in the wakes increases downstream of this location as the wake continues to spread and thicken. As plotted in Fig. 7(a), the velocity decrement decreases as x increases.

Nondimensional static and total pressure coefficients for this baseline configuration at $\alpha = 0$ deg and $Re = 1.00 \times 10^6$ are presented in Fig. 8. The chord-normal pressure gradient $\partial p/\partial \widetilde{y}$ is visible in Fig. 8(a) which causes curvature in the flowfield as the flowfield returns to the freestream condition ($u = U_\infty$, $v = w = 0$), and also contributes to asymmetric wake development. As seen in the figure, It is evident that $\partial p/\partial \widetilde{y}$ is clearly non-zero and this observation may indicate that the boundary layer equations, whereby $\partial p/\partial \widetilde{y} = 0$ is assumed, may not be applied with reasonable accuracy for large, thick wakes such as those observed in this research.

Figure 8(b) shows $C_{p,t}$, or the nondimensional loss of total pressure as defined by Eq. 21, which provides a clear visualization of the wake. As expected, trends in $C_{p,t}$ are closely mirrored by the trends observed in $\widetilde{U_t}$. The largest

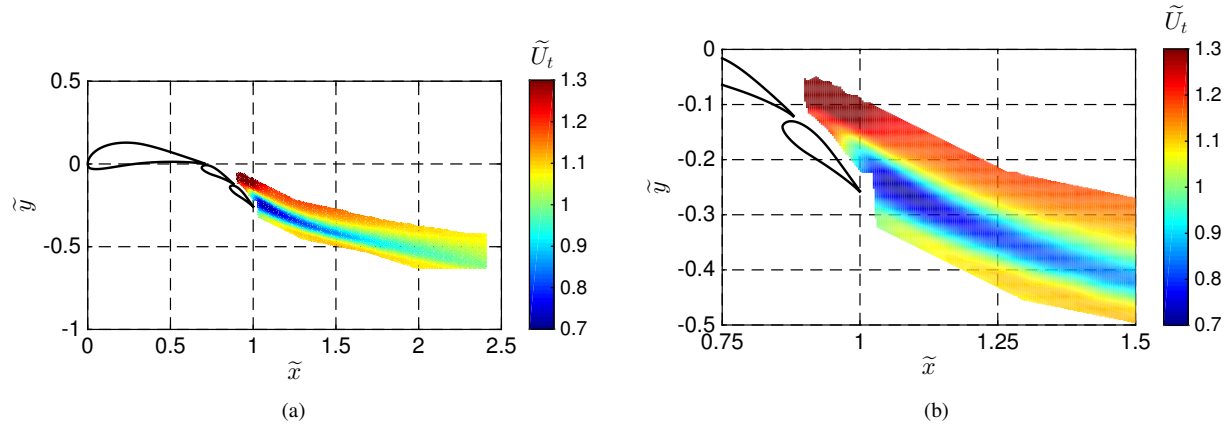

Figure 7. Total velocity ($\widetilde{U}_t$) for Configuration 10 at $\alpha = 0$ deg and $Re = 1.00 \times 10^6$ shown at a) wide view and b) detailed view.

decrements in $C_{p,t}$ are observed just downstream of the trailing edge of flap 2, and the magnitude of the minimum value of $C_{p,t}$ at a given $\widetilde{x}$ decreases with increasing downstream distance. As the wake thickens with increased downstream distance, the magnitude of $C_{p,t}$ must decrease in the wake to maintain the same total integrated momentum deficit. A small, thin wake yields a more-negative value of $C_{p,t}$ than a large, thick wake. In addition, it is observed that the magnitude of $\partial C_{p,t}/\partial \widetilde{y}$ is larger along the lower wake edge than the upper wake edge. It is evidenced by the fact that the upper wake edge begins to spread out rapidly downstream of $\widetilde{x} \approx 1.25$ while this behavior is not observed along the lower wake edge. These observations are visualized by the magnitude of the gradients of $\partial C_{p,t}/\partial \widetilde{y}$ in which the lower wake edge appears as a thinner shear layer in Fig. 8(b) than the upper wake edge.

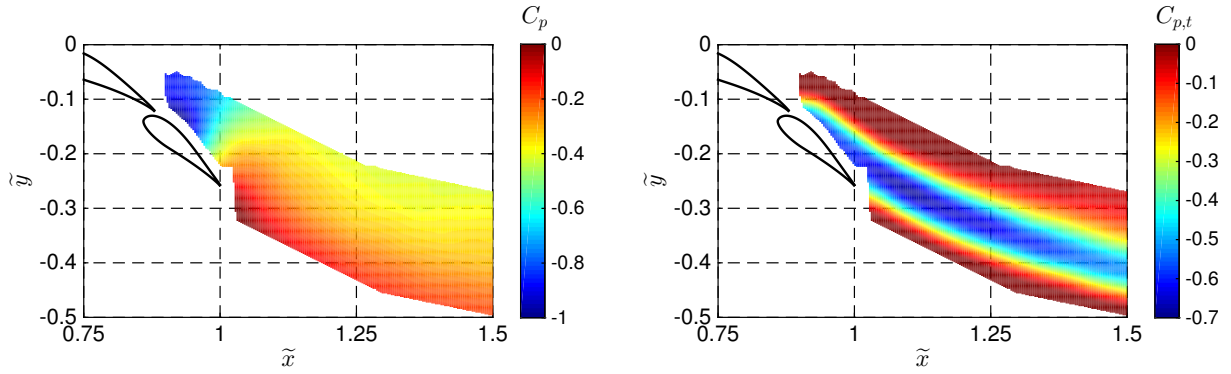

Figure 8. Nondimensional pressure results for Configuration 10 at $\alpha = 0$ deg and $Re = 1.00 \times 10^6$ including a) C_p and b) $C_{p,t}$.

In an effort to quantify the extent to which a wake is burst, a figure of merit based upon the previously discussed $C_{p,t}$ is developed. As defined in Eq. 21, $C_{p,t}$ is a nondimensional measure of the difference between the local total pressure and the freestream total pressure where values of $C_{p,t} < 0$ indicate that the local flowfield has less total head than that of the freestream condition. Points in the wake were numerically determined in which the local $C_{p,t}$ was less than a threshold value, selected to be -0.10 in this research. Thus, at a constant $\widetilde{x}$ location, a range of $\widetilde{y}$ values exist for which

$$C_{p,t} \leq -0.10 \tag{22}$$

The figure of merit, h_w, is defined to be the distance between the minimum and maximum values in $\widetilde{y}$ at a given $\widetilde{x}$ for which Eq. 22 is satisfied, or

$$h_w = \widetilde{y_u} - \widetilde{y_l} \tag{23}$$

The figure of merit can be calculated with any threshold value, but -0.10 is selected for results in this paper. Ideally, the wake edges could be defined by the outer-most points for which $C_{p,t} < 0$. However, as seen in Fig. 8(b), not all of these points were captured in the wake survey, especially at large values of $\widetilde{x}$. Thus, to provide a clear comparison

between different geometric configurations, the figure of merit as defined in Eqs. 22–23 was selected. Baseline results for h_w at $Re = 1.00 \times 10^6$ and $\alpha = 0$ deg are plotted in Fig. 9(a), and the computed edges for which $C_{p,t} < -0.10$ are coplotted with $C_{p,t}$ and U_t in Fig. 9(b,c). As seen in Fig. 9(a), h_w generally increases with downstream distance, which is the expected trend. The wake is observed to thicken with downstream distance due to both the streamwise pressure gradient and the increase in downstream distance. Results indicate that h_w increases by nearly 30% from $\widetilde{x} \approx 1.0$ to $\widetilde{x} \approx 2.0$. It is noted that a small decrease in h_w is observed just downstream of the trailing edge of flap 2 at $\widetilde{x} \leq 1.1$. In this region, large pressure gradients, both in the x and in the y directions, are observed, as shown in Fig. 8(a). It is unknown why this reduction in h_w is observed immediately downstream of the system trailing edge. Nevertheless, it must be stated that the calculated wake edges are not the same as streamlines for the flowfield. If the wake edges were streamlines, a reduction in the distance between two streamlines would indicate an accelerating flowfield. However, this is not the case with the wake edges as they are not defined by streamlines.

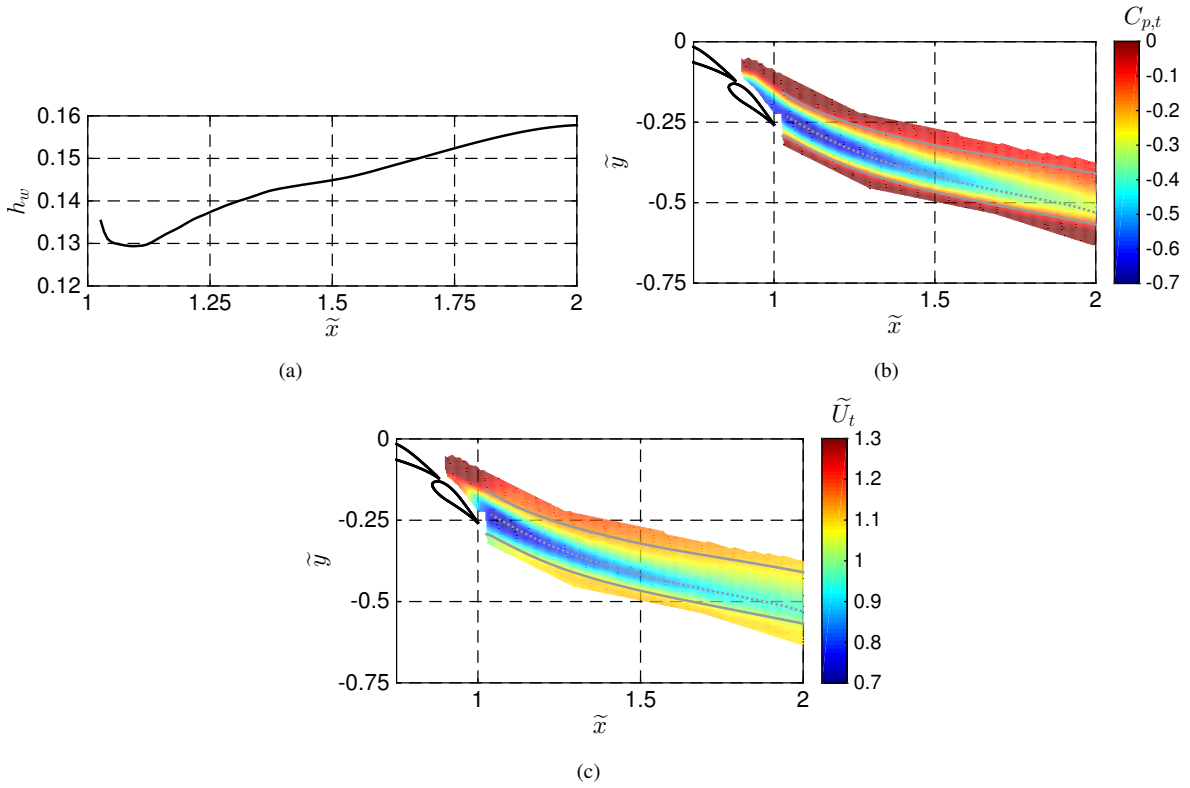

Figure 9. Wake edge results for Configuration 10 at $Re = 1.00 \times 10^6$ and $\alpha = 0$ deg including a) wake thickness (h_w), b) $C_{p,t}$ coplotted with wake edges and c) U_t coplotted with wake edges.

At a given value of $\widetilde{x}$, the point of minimum $C_{p,t}$ was extracted, and this point is defined as the peak $C_{p,t}$ point (denoted by $\widetilde{y}_{peak}$). As previously mentioned, the velocity and total pressure distributions are asymmetric with respect to y, and these distributions are different on either side of the wake peak. Both the peak point and the bounding edges to calculate h_w, are plotted in Fig. 10(a). Results indicate that the peak point is closer to y_l than y_u, and that the peak moves closer to y_l with increasing downstream distance. Results in Fig. 10(b) present the wake-normalized value $(\widetilde{y}_{peak} - \widetilde{y}_l)/h_w$ in which a value of 0 corresponds to $\widetilde{y}_l$ while a value of 1 is equal to $\widetilde{y}_u$. This parameter indicates that the wake peak is close to the center of the wake at small values of $\widetilde{x}$, but that the peak moves closer to $\widetilde{y}_l$ with increasing downstream distance. Overall, the asymmetry in the flowfield is caused by the curvature in the flowfield. As lift is a result of the flowfield curvature, it is surmised that different flowfield conditions (yielding different values of C_l) would affect the asymmetry in various manners. In addition, differing streamwise pressure gradients would affect the growth rate of wakes in different manners, and this topic will be investigated in the next section.

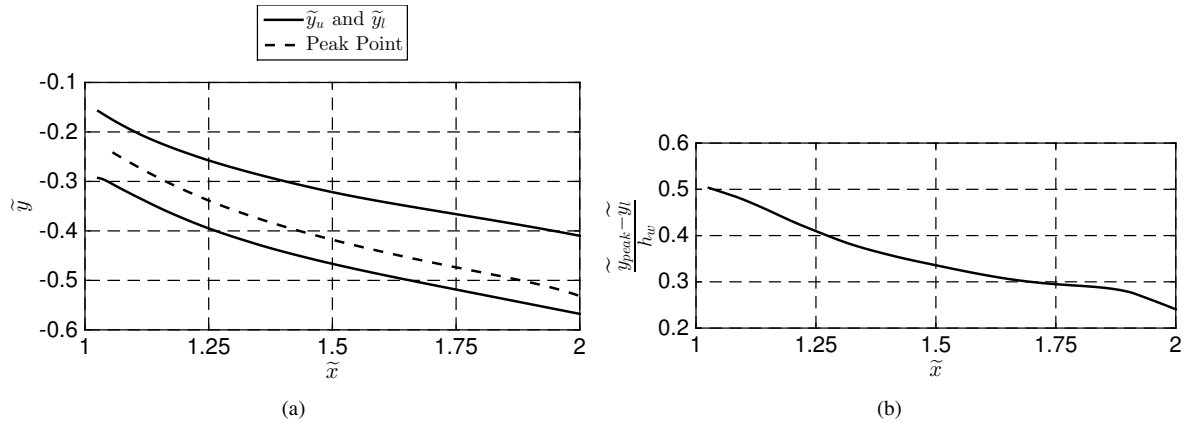

Figure 10. Wakes as evidenced by a) dimensional $\widetilde{y}_l$, $\widetilde{y}_u$, and peak points (location of minimum $C_{p,t}$) and b) normalized peak points.

B. Angle of Attack

Because flowfields at a higher α experience stronger adverse pressure gradients in the pressure-recovery region, it was expected that the burst wakes at two different α values would be different. To test this hypothesis, data were acquired for the Configuration 10 at α ranging between -3 and 0 deg. Wake surveys were captured for each of these conditions, and h_w was calculated for each of these cases, as shown in Fig. 11(a). Significant differences in h_w are observed for these cases, and it is clear that thinner wakes are observed at decreased α than at larger values of α. As previously discussed and as shown in Fig. 7(b), the wake from the main element and flap 1 merge and interact to the point where a clear division, or central core, of the two wakes is not evident. This trend was also observed for decreased α, as shown in Fig. 11(b). Results at all α presented indicate a decrease in h_w immediately downstream of the trailing edge of the system, as shown in the figure and previously discussed. At points for which $\widetilde{x} > 1.20$, an increase in h_w is observed for larger α while a decrease in h_w is seen for smaller α. While the wakes were all observed to thicken with increased downstream distance, the value of h_w did not necessarily always thicken with larger x. A reduction in the streamwise adverse pressure gradient at decreased α yielded smaller, thinner wakes than the wakes in flowfields at larger α. Because of the reduced pressure gradient at lower α, the wakes were observed to burst less and contain fewer points in which $C_{p,t} < -0.10$. Curiously, despite the fact that an decrease in α yields reduced adverse pressure gradients, the minimum value of U_t differs by only 2% of freestream U_t ($U_{t,min}|_{\alpha=0} = 0.70$ and $U_{t,min}|_{\alpha=-3} = 0.68$). Overall, results indicate that an increase in α yields increased wake bursting as measured by the h_w figure of merit.

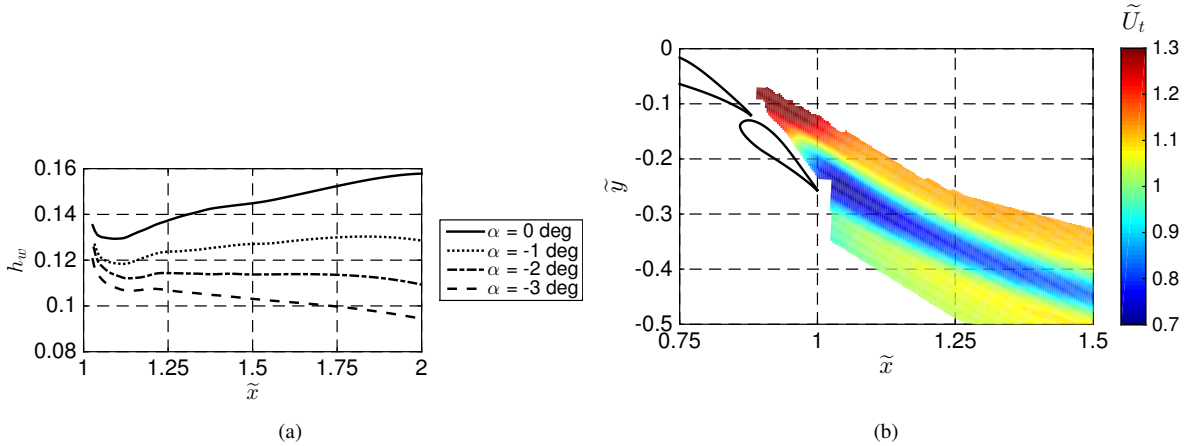

Figure 11. Effect of α on burst wakes as evidenced by a) h_w for varying α and b) U_t at $\alpha = -3$ deg.

C. Gap Size

Two additional configurations were tested that had different gap sizes than the baseline Configuration 10, as defined in Table 1. Configurations 15 and 16, contained larger (2.0%) and smaller (0.50%) gap sizes, respectively, relative to the baseline geometry. As discussed in the introduction, the effect of gap sizes on multielement airfoils has been documented, and typical gap sizes are between 1.3% and 2.0%. Wake survey results for the three different configurations ($gap_{1,2} = 0.50\%$, 1.00%, and 2.00%) are shown in Fig. 12. Results indicate that the burst point, or the location at which rapid thickening of the wake is first observed, moves slightly downstream with increasing gap size. In addition, the minimum velocity is observed to decrease as the gap size increases, and increased merging of the two wakes is observed. Some trailing edge separation is present in Configuration 16 ($gap_{1,2} = 0.50\%$), and this observation has been confirmed through surface oil flow visualization. Thus, reduction in gap size may cause an airfoil to be more prone to separation than a configuration with larger gap sizes. Configurations with a larger gap size exhibit two distinct wakes and less merging between the wakes than that of a smaller gap size. In particular, Configuration 15, shown in Fig. 12(c), shows three distinct wakes. The three wakes are generated by the main element, flap 1, and flap 2, and the wakes have not merged into one wake. As the wakes have not full merged, the definition of h_w in Eq. 23 is not easily applied to Configuration 15. However, wake thickness, as measured by the h_w figure of merit, is presented in Fig. 12(d) for Configurations 10 and 16. The data indicate that a reduction in gap size has a minimal effect on the wake thickness, and that growth rates are similar for the two configurations. It must be recalled, however, that the wake of Configuration 16 is affected by the trailing-edge separation of flap 2, so it is difficult to make comparisons between the burst wake of Configuration 10 and the separated wake of Configuration 16. All of these observations suggest that a configuration with a larger gap size yields less wake bursting than that of a configuration with a smaller gap size while a reduction in gap size may cause the flow to separate make a flowfield more prone to separation.

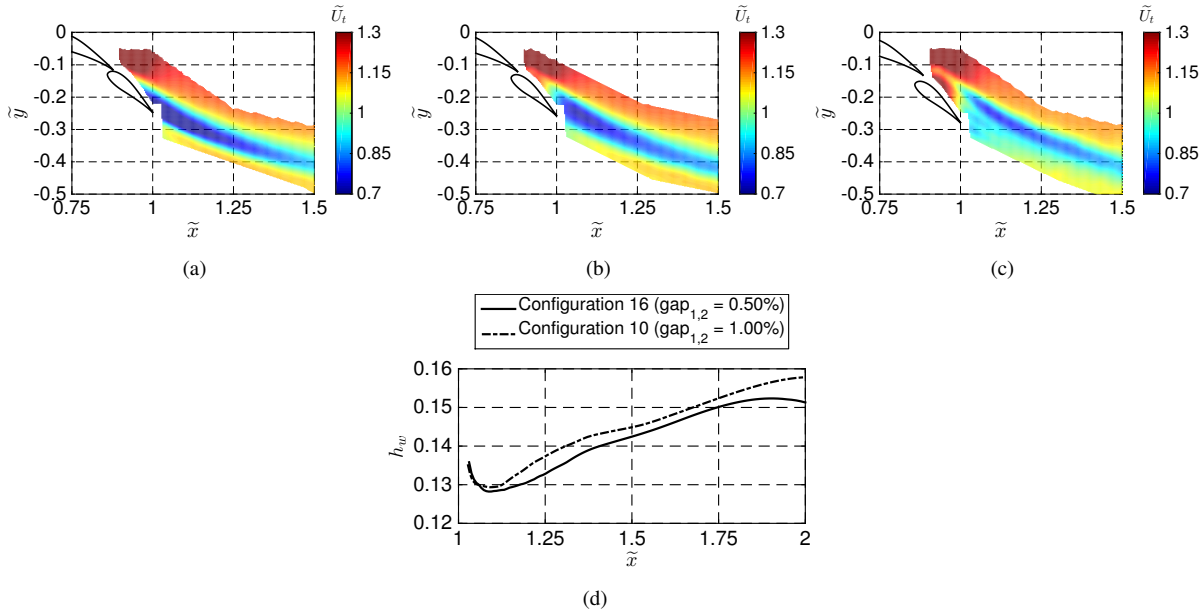

Figure 12. Effect of gap size on burst wakes including a) Configuration 16 ($gap_{1,2} = 0.50\%$), b) Configuration 10 ($gap_{1,2} = 1.00\%$), c) Configuration 15 ($gap_{1,2} = 2.00\%$) and d) wake thickness as defined by h_w.

D. Overhang Distance

A comparison of Configurations 10 and 13 captured the effect of a reduction in overhang distance. As defined in Fig. 3(a), a reduction in overhang distance corresponds to a flap which is moved downstream relative to a baseline configuration. (In other words, the flap is not tucked under the previous element as much as the original case.) The figure of merit for wake thickness, h_w, for the two configurations is plotted in Fig. 13(c). The growth rate of both wakes is negative immediately after the trailing edge of the system, but the wakes then thicken as $\widetilde{x}$ increases. A thicker wake is observed for the configuration in which $overhang_{1,2} = +1.50\%$ than that of $overhang_{1,2} = 0.00\%$. An examination of the wake survey results indicates less momentum deficit is observed with an overhang of 0.00% than that of a configuration in which $overhang = 1.50\%$. In addition, the region of the wake in which $\widetilde{U}_t < 0.70$ is observed to be

smaller and further upstream for Configuration 13 than for Configuration 10. The burst point is essentially unchanged for the two configurations. The figure of merit h_w for the two configurations is plotted in Fig. 13(c), and data suggest that a larger overhang distance causes a thicker wake than a configuration with smaller overhang distance. It is noted that the typical reduction in h_w is present immediately downstream of the trailing edge of the system after which the wake thickens with increasing downstream distance. A reduction in h_w for Configuration 13 at $\widetilde{x} \approx 1.85$ indicates this wake has less total head loss in the central portion of the wake, and therefore less wake bursting overall, than Configuration 10. All of these observations indicate it can be generally stated that a larger overhang distance yields more wake bursting than a configuration with a smaller overhang distance.

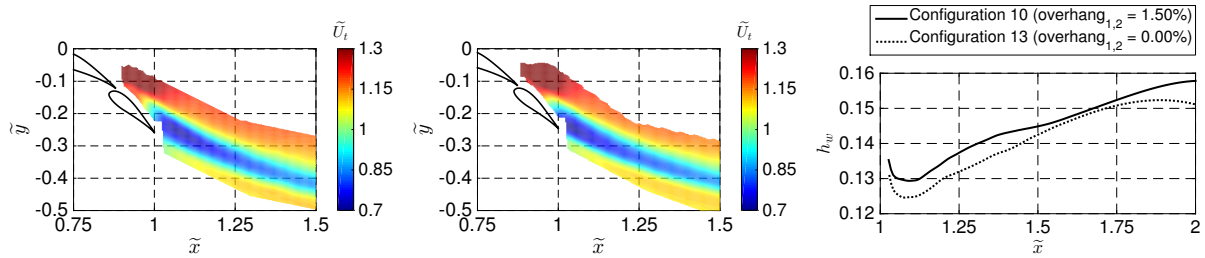

Figure 13. Effect of overhang distance on burst wakes including a) Configuration 10 ($overhang_{1,2} = 1.50\%$), b) Configuration 13 ($overhang_{1,2} = 0.00\%$), and c) wake thickness as defined by h_w.

E. Deflection Angle

The final parameter in the relative coordinate system is δ_r, or the relative deflection angle between two elements. The effect of δ_r was captured by comparing Configurations 10 and 11, as defined in Tables 1 and 2. As larger flap deflections yield stronger adverse pressure gradients, the burst wakes are considerably different between the two cases, as plotted in Fig. 14. As seen in the figure, a reduction in flap deflection yields yields less wake bursting than for a configuration with increased flap deflection angle. Wake thickness for both configurations is plotted in Fig. 14(c). Both configurations exhibit the typical decrease in h_w immediately downstream of the trailing edge of the system, and both grow after this initial decrease. It is interesting to note the wake development of Configuration 11 (dashed line), which has decreased δ_r relative to the baseline configuration. While h_w initially grows for Configuration 11, the growth rate is significantly smaller than that of Configuration 10. An increase in h_w of approximately 10% is observed until $\widetilde{x} \approx 1.65$ after which the growth rate is negative. In contrast, a negative growth rate is not observed for Configuration 10. The wake for Configuration 11 continues to decrease up to $\widetilde{x} = 2.0$.

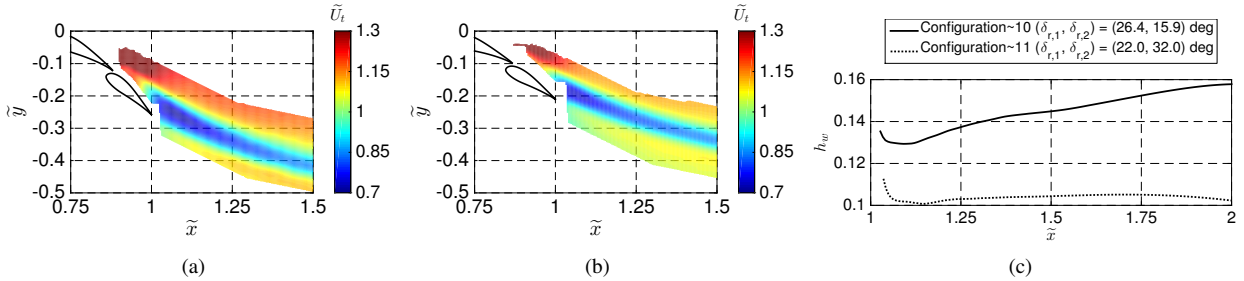

Figure 14. Effect of flap deflection angle on burst wakes including a) Configuration 10 (increased δ), b) Configuration 11 (decreased δ), and c) wake thickness as defined by h_w.

V. Conclusions

Experimental data were collected using off-body measurement techniques for burst wakes in a multielement airfoil flowfield which included adverse pressure gradients and flow curvature. A 7-hole probe was used to determine velocity, static pressure, and total pressure. A baseline configuration was studied in extensive detail, and it was concluded that an increase in α leads to thicker wakes with increased momentum deficit relative to a baseline configuration. A figure of merit is proposed which quantifies the extend to which a wake is burst, and this parameter is used to compare wakes

for different freestream flow conditions or different flap riggings. It was found that a smaller gap size, larger overhang distance, and increased flap deflection angle all increased the "strength" of wake bursting, as measured by this figure of merit.

Acknowledgments

Support for this research project was provided by National Science Foundation graduate research fellowship grant number 07-15088 and the UIUC Department of Aerospace Engineering. The authors would like to extend appreciation to Jeffrey Diebold and Robert Deters for numerous insightful and rewarding discussions regarding the operation and calibration of the 7-hole probe.

References

[1]Mack, M. D. and McMasters, J. H., "High Reynolds Number Testing in Support of Transport Airplane Development," AIAA Paper 92-3982, AIAA Aerospace Ground Testing Conference, Nashville, TN, 1992.

[2]Smith, A. M. O., "High-Lift Aerodynamics," *Journal of Aircraft*, Vol. 12, No. 6, 1975, pp. 501–530.

[3]van Dam, C. P., "The Aerodynamic Design of Multi-Element High-Lift Systems for Transport Airplanes," *Progress in Aerospace Sciences*, Vol. 38, 2002, pp. 101–144.

[4]Nakayama, A., Kreplin, H. P., and Morgan, H. L., "Experimental Investigation of Flowfield About a Multielement Airfoil," *AIAA Journal*, Vol. 28, No. 1, 1988, pp. 14–21.

[5]Driver, D. M. and Mateer, G. G., "Wake Flow in Adverse Pressure Gradient," *International Journal of Heat and Fluid Flow*, Vol. 23, 2002, pp. 564–571.

[6]Hoffenberg, R. and Sullivan, J. P., "Measurement and Simulation of Wake Deceleration," AIAA Paper 98-0522, AIAA Aerospace Sciences Meeting, Reno, NV, 1998.

[7]Pomeroy, B. W., Ansell, P. J., Diebold, J. M., and Selig, M. S., "A Study of Burst Wakes in a Multielement Airfoil Flowfield," AIAA Paper 2013-2919, AIAA Applied Aerodynamics Conference, San Diego, CA, 2013.

[8]Pomeroy, B. W., Diebold, J. M., Ansell, P. J., and Selig, M. S., "Study of Burst Wakes in a Multielement Airfoil Flowfield," *AIAA Journal*, Vol. 52, No. 4, April 2014, pp. 821–831.

[9]Klausmeyer, S. M. and Lin, J. C., "An Experimental Investigation of Skin Friction on a Multi-Element Airfoil," AIAA Paper 94-1870, AIAA Applied Aerodynamics Conference, Colorado Springs, CO, 1994.

[10]Hoffenberg, R. and Sullivan, J. P., "Simulation of High-Lift Wake Behavior," AIAA Paper 97-0718, AIAA Aerospace Sciences Meeting, Reno, NV, 1997.

[11]Spaid, F. W., "High Reynolds Number, Multielement Airfoil Flowfield Measurements," *Journal of Aircraft*, Vol. 37, No. 3, 2000, pp. 499–507.

[12]Rogers, S. E., "Progress in High-Lift Aerodynamic Calculations," *Journal of Aircraft*, Vol. 31, No. 6, 1994, pp. 1244–1251.

[13]Valarezo, W. O., Dominik, C. J., and McGhee, R. J., "Multielement Airfoil Performance Due to Reynolds and Mach Number Variations," *Journal of Aircraft*, Vol. 30, No. 5, 1993, pp. 689–694.

[14]Pomeroy, B. W., Williamson, G. A., and Selig, M. S., "Experimental Study of a Multielement Airfoil for Large Wind Turbines," AIAA Paper 2012-2892, AIAA Applied Aerodynamics Conference, New Orleans, LA, 2012.

[15]Cebeci, T., Besnard, E., and Chen, H. H., "Calculation of Multielement Airfoil Flows, Including Flap Wells," AIAA Paper 96-0056, AIAA Aerospace Sciences Meeting, Reno, NV, 1996.

[16]Czerwiec, R. and Edwards, J. R., "Theory and Experiment of Multielement Airfoils – A Comparison," AIAA Paper 2000-0985, AIAA Aerospace Sciences Meeting, Reno, NV, 2000.

[17]Narsipur, S., Pomeroy, B. W., and Selig, M. S., "CFD Analysis of Multielement Airfoils for Wind Turbines," AIAA Paper 2012-2781, AIAA Applied Aerodynamics Conference, New Orleans, LA, 2012.

[18]Wang, G., Liu, Y., Mian, H. H., and Ye, Z.-Y., "A NUFFT Technique for Flow Fluctuation Analysis Based on the Unsteady Flow Simulation with Variable Physical Time Stepping Scheme," AIAA Paper 2014-3251, AIAA Applied Aerodynamics Conference, Atlanta, GA, 2014.

[19]Chin, V. D., "Flowfield Measurements about a Multi-Element Airfoil at High Reynolds Numbers," AIAA Paper 93-3137, AIAA Fluid Dynamics Conference, Orlando, FL, 1993.

[20]Schneider, S., Campbell, B., Bucci, G., and Sullivan, J. P., "An Experimental Simulation of Flap Flow on Multielement Airfoils at High Reynolds Number," AIAA Paper 94-2613, AIAA Aerospace Ground Testing Conference, Colorado Springs, CO, 1994.

[21]Hoffenberg, R., Sullivan, J. P., and Schneider, S., "Wake Measurements in a Strong Adverse Pressure Gradient," NASA CR 197272, 1995.

[22]Bucci, G. S. and Sullivan, J. P., "An Experimental Simulation of High Lift Wake Flows at High Reynolds Number," AIAA Paper 97-2297, AIAA Applied Aerodynamics Conference, Atlanta, GA, 1997.

[23]Ragheb, A. M. and Selig, M. S., "Multi-Element Airfoil Configurations for Wind Turbines," AIAA Paper 2011-3971, AIAA Applied Aerodynamics Conference, Honolulu, HI, 2011.

[24]Khodadoust, A., *An Experimental Study of the Flowfield on a Semispan Rectangular Wing with a Simulated Glaze Ice Accretion*, Ph.D. thesis, Department of Aerospace Engineering, University of Illinois at Urbana-Champaign, Urbana IL, 1993.

[25]Barlow, J. B., Rae, W. H., Jr., and Pope, A., *Low-Speed Wind Tunnel Testing*, Wiley-Interscience, New York, NY, 3rd ed., 1999, pp 328-346.

[26]Gallington, R. W., "Measurement of Very Large Flow Angles with Non-Nulling Seven-Hole Probes," Department of Aeronautics, United States Air Force Academy, Colorado Springs, CO, USAFA-TR-80-17, 1980.

[27]Gerner, A. A., Maurer, C. L., and Gallington, R. W., "Non-Nulling Seven-Hole Probes for High-Angle Flow Measurement," *Experiments in Fluids*, Vol. 2, No. 2, 1984, pp. 95–103.

[28]Crawford, J. D., *Design and Calibration of Seven-Hole Probes for Flow Measurement*, Master's thesis, Department of Mechanical and Materials Engineering, Queen's University, Kingston Ontario Canada, 2011.

[29]Zilliac, G. G., "Calibration of Seven-Hole Pressure Probes for Use in Fluid Flows with Large Angularity," NASA TM 102200, 1989.

[30]Zilliac, G. G., "Modelling, Calibration, and Error Analysis of Seven-Hole Pressure Probes," *Experiments in Fluids*, Vol. 14, 1993, pp. 104–120.

[31]Deters, R. W., *Performance and Slipstream Characteristics of Small-Scale Propellers at Low Reynolds Numbers*, Ph.D. thesis, Department of Aerospace Engineering, University of Illinois at Urbana-Champaign, Urbana IL, 2014.